

Near-Infrared Quantum Emission from Oxygen-Related Defects in hBN

Sean Doan,^{1,*} Sahil D. Patel,^{2,*} Yilin Chen,³ Jordan A. Gusdorff^{4,5} Mark E. Turiansky,⁶ Luis Villagomez,² Luka Jevremovic,² Nicholas Lewis,² Kenji Watanabe,⁷ Takashi Taniguchi,⁸ Lee C. Bassett,⁴ Chris Van de Walle,³ and Galan Moody^{2,†}

¹*Physics Department, University of California, Santa Barbara, CA 93106, USA*

²*Electrical and Computer Engineering Department, University of California, Santa Barbara, CA 93106, USA*

³*Materials Department, University of California, Santa Barbara, CA 93106, USA*

⁴*Electrical and Systems Engineering Department, University of Pennsylvania, Philadelphia, PA, 19104, USA*

⁵*Materials Science and Engineering Department, University of Pennsylvania, Philadelphia, PA, 19104, USA*

⁶*US Naval Research Laboratory, 4555 Overlook Ave SW, Washington, DC 20375, USA*

⁷*Research Center for Functional Materials, National Institute for Materials Science, 1-1 Namiki, Tsukuba 305-004, Japan*

⁸*International Center for Materials Nanoarchitectures, National Institute for Materials Science, 1-1 Namiki, Tsukuba 305-004, Japan*

(Dated: December 19, 2025)

Color centers hosted in hexagonal boron nitride (hBN) have emerged as a promising platform for single-photon emission and coherent spin–photon interfaces that underpin quantum communication and quantum networking technologies. As a wide-bandgap van der Waals material, hBN can host individual optically active quantum defects emitting across the ultraviolet to visible spectrum, but existing color centers often show broad phonon sidebands (PSBs), unstable emission, or inconvenient wavelengths. Here, we show a simple, scalable oxygen-plasma process that reproducibly creates oxygen-related single quantum emitters in hBN with blinking-free zero-phonon lines spanning the near-infrared (NIR) spectrum from 700–960 nanometers. These emitters demonstrate room-temperature operation, high brightness, and ultra-sharp cryogenic linewidths in the few-gigahertz range under non-resonant excitation. Analysis of the PSBs shows weak electron-phonon coupling and predominant zero-phonon-line emission, while first-principles calculations identify plausible oxygen-related defect configurations. These emitters provide a promising platform for indistinguishable NIR single photons towards free-space quantum networking.

INTRODUCTION

Color centers in hexagonal boron nitride (hBN) are an emerging platform for single-photon sources and coherent spin-photon interfaces that are essential for quantum communication and quantum networking [1, 2]. Being a wide bandgap semiconducting van der Waals (vdW) material, hBN has high thermal and chemical stability, making it a robust material for use in ambient conditions similar to more established materials such as diamond [3]. Due to its wide bandgap energy (~ 6 eV), hBN can host a variety of optically active defects that emit from the ultraviolet (UV) to near infrared (NIR) [4–6]. These color centers have spatially localized electronic structures with transition energies within the bandgap that enable quantum light generation.

The layered structure of hBN offers unique advantages compared to other materials by ensuring that its defects are two-dimensional (2D) in nature and are able to function at surfaces, devoid from any surface states, allowing

for strong proximity interaction with their surrounding environment and optimal single-photon emission [7–9]. Furthermore, hBN has been demonstrated to have exceptionally high photon extraction efficiencies [10, 11] due to its atomic thickness, site-controlled and deterministic manufacturability [5, 12, 13], and the ability to be integrated with optoelectronic, photonic, and acoustic technologies via simple transfer methods [14–17]. Color centers in hBN have also exhibited single-photon and spin-optical signatures at both ambient conditions and cryogenic temperatures [5, 6, 18–20] making them strong candidates for realizing spin-photon interfaces, quantum photonic sources, and quantum sensors.

Despite these attractive attributes, the specific defect families identified to date each exhibit several drawbacks, including modest internal quantum efficiency, pronounced phonon sidebands, broad optical linewidths, or operational wavelengths not amenable to free space or fiber transmission [21–23]. This necessitates the search for other potential color centers in hBN that have optimal single-photon emission in the NIR spectrum with high internal quantum efficiencies and signatures of spin-photon coupling.

In this work, we present a novel oxygen-plasma pro-

* These authors contributed equally to this work.

† mooody@ucsb.edu

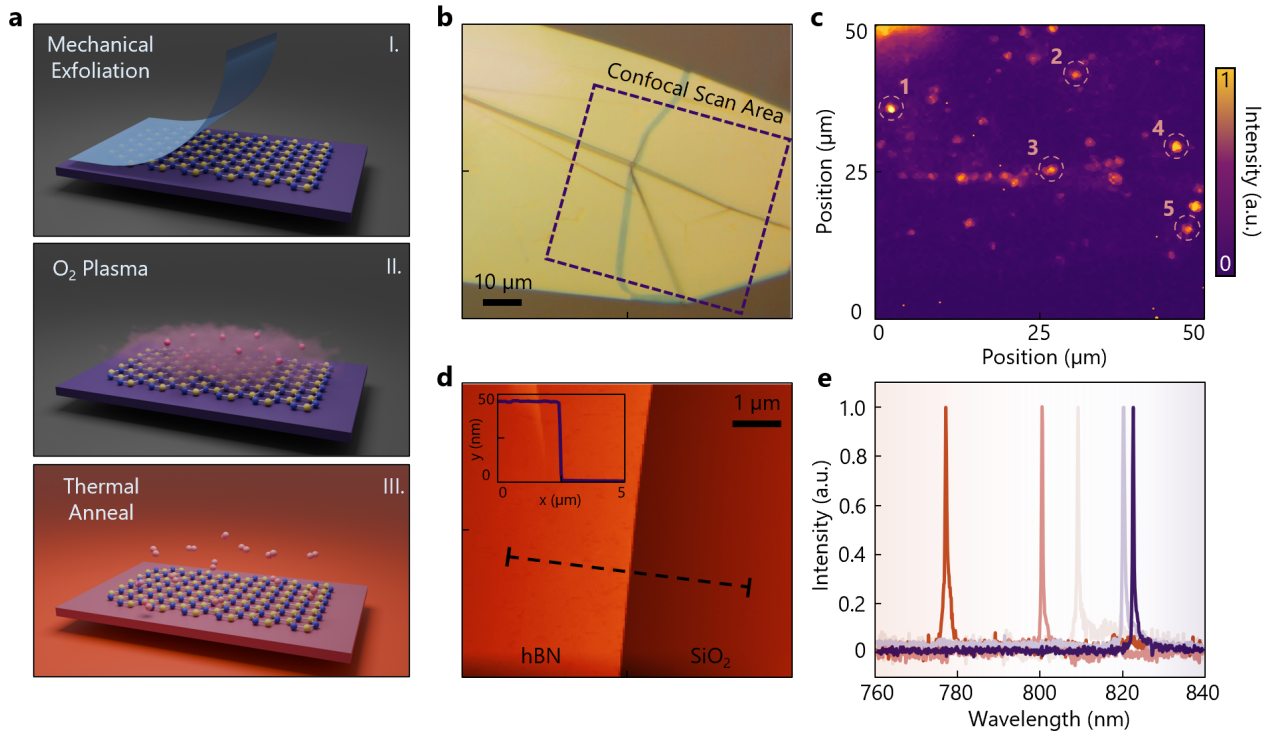


FIG. 1. Fabrication process and overview of generated NIR SQE's. (a) Schematic illustration of the fabrication process for generating NIR SQEs. Panel I denotes a mechanical exfoliation method to create sub-100 nm hBN samples. Panel II denotes an oxygen plasma treatment to introduce oxygen-related defects into the hBN lattice. Panel III denotes a thermal anneal process to stabilize the SQE within the hBN. (b) An optical micrograph of a processed hBN sample. The dashed line indicates the area of a photoluminescence (PL) confocal map. (c) A confocal hyperspectral PL map of the processed hBN sample showcasing spatially resolved single-emitters across the sample. (d) An atomic force microscopy (AFM) image is shown, highlighting the smooth surface topography of the hBN remains intact after the plasma treatment and processing. The inset shows a line scan across the dashed line and indicates a sample thickness of 50 nm. (e) Representative PL spectra of the generated spatially isolated NIR SQEs. Spectra of SQEs 1-5 in panel (c) are shown from left to right, respectively. SQEs are observed over a wide range of wavelengths spanning from 700 nm to 960 nm.

cess that reproducibly generates bright and stable NIR oxygen-related single quantum emitters (SQE) in hBN. From hyperspectral confocal maps of over 200 sites, we show that these defect complexes display narrow blinking-free zero-phonon lines (ZPLs) spanning 700–960 nm, room-temperature emission, and ultrasharp cryogenic linewidths as low as 2.7 GHz. At 4 K, they achieve brightnesses approaching 1 MHz without photonic cavity enhancement, exhibit pronounced single-photon antibunching, low Huang-Rhys factors with weak vibronic coupling, and both high emission and absorption dipole visibility. Detailed power and temperature dependent linewidth analysis under non-resonant and quasi-resonant excitation further sheds light on broadening mechanisms of the ZPL. Using first-principles calculations and screening of oxygen-related defects by ZPL energy and vibronic coupling, we identify O_NV_N and O_NV_NH centers as the most plausible defect complexes with both systems being paramagnetic with spin doublets indicating potential spin-dependent optical manipulation. These NIR SQEs offer a promising pathway to indistinguishable single photons, spin-optical interfaces, and free-space NIR quantum communication and networking platforms in hBN.

RESULTS

Defect Metrology. Our oxygen-plasma defect creation process is illustrated in Fig. 1 and detailed in the Methods section. To rigorously characterize the creation of these NIR SQEs, we have performed this fabrication across many thin hBN flakes, including control experiments to confirm the defect formation under oxygen plasma treatment.

Figure 1b displays an optical micrograph of a representative processed hBN flake of ~50 nm thickness undergoing the outlined fabrication procedure. The dashed box represents the hyperspectral confocal photoluminescence (PL) mapping scan area performed at 4 K which is shown in Fig. 1c. We observe high density generation of localized hotspots corresponding to single defect SQEs that emit in the NIR spectrum across a wide range of hBN flake thicknesses from 15-100 nm. Across 5 processed hBN flakes, we estimate a SQE area density of $2 \times 10^6 \text{ cm}^{-2}$ indicating a high yield of SQE generation across a given hBN flake. We note that we only observe a strong NIR emission from such single defects with the inclusion of the oxygen-plasma treatment. Control experiments were performed with the absence of the oxygen-plasma

treatment while maintaining the standard mechanical exfoliation and rapid thermal anneal (RTA) procedure and no NIR emission was observed (Supplementary Note 1). Combined with the theoretical evaluation of a proposed defect complex (see Fig. 5), this leads us to assign such distinct emission to be oxygen-related.

To analyze the surface topography of the processed hBN, we perform atomic force microscopy (AFM) and obtain AFM topography maps of the surface of multiple processed hBN flakes. Fig. 1d shows a representative topography map of the processed hBN flake displayed in Fig. 1b with an atomic thickness shown in the step profile (inset, line cut taken along dashed line in Fig. 1d). Here, we extract an RMS surface roughness of 405.6 pm across the flake indicating the hBN surface remains relatively smooth and undamaged from the fabrication process allowing for generation of clean-interfaced 2D heterostructures and potential integration into optoelectronic and photonic devices. We observe a similar structural integrity and smooth surface topography across multiple samples used for this work.

Furthermore, we see strong correlation between multiple hBN samples of these single defects being localized near hBN cracks, terraces, and folds that form prior to the plasma and RTA treatment. Such features are natural occurrences from the mechanical exfoliation process. This indicates a further correlation between these SQEs forming in areas of localized strain fields, irregular crystal symmetries, or a combination of both, which has been demonstrated in other types of defect complexes in hBN and other 2D materials [24–26].

Cryogenic Photophysics. We next analyzed the spectral properties of the generated oxygen-related NIR SQEs. We obtain individual PL spectra from isolated single defects at 4 K indicated in Fig. 1e. Additional analysis on the room-temperature emission can be found in Supplementary Note 2. Notably, these SQEs exhibit sharp linewidths at cryogenic temperatures and span into the NIR wavelength range, making them highly suitable for free-space optical-based applications due to minimal atmospheric absorption losses in this spectral band [27].

To verify the antibunching nature of these single-defect SQEs, we perform Hanbury Brown and Twiss (HBT) interferometry. We record the second-order photon correlation function $g^2(\tau)$ obtained under continuous laser (CW) excitation at 660 nm. The result is presented in Fig. 2b of a representative SQE, which demonstrates a single photon antibunching dip at zero delay time. We used the single exponential function: $g^2(\tau) = 1 - \alpha e^{(-|\tau|/\tau_0)}$ to fit the experimental data, resulting in a raw value of 0.23 ± 0.09 (0.18 ± 0.09 instrument response function (IRF) corrected) at zero time delay, indicating predominantly single photon emission from our NIR SQEs.

To investigate the photostability, we recorded spectra for 1 minute with a 1 second integration time for each frame to examine possible slow time scale spectral diffusion, blinking, or photobleaching effects. The resulting spectral trajectory of a representative NIR SQE with a ZPL of 767 nm (Supplementary Note 3) indicates a slight spectral diffusion on one-second time scales and a blinking-free emission. This spectral diffusion is comparable to other types of single defect complexes typically observed under non resonant optical pump conditions [28, 29]. We observe a reduction in spectral diffusion at lower excitation powers far from saturation, which improves the photostability (Supplementary Note 3). To reduce this slow-time scale diffusion, the photostability can be enhanced through further defect engineering methods such as surface passivation and active stabilization techniques [30, 31].

Next, the intensity of the same SQE versus the excitation pump power is measured to examine power broadening (Supplementary Note 3). The integrated intensity of the SQE clearly shows a saturation behavior, which is the typical signature of an individual two-level system. We fit the data to a first-order saturation model [32], $I = I_{sat}P/(P + P_{sat})$, to fit the background corrected experimental data points, where P_{sat} and I_{sat} are the saturated excitation laser power and intensity, respectively. The best fit to the experimental data yields a saturation power of 1.1 mW and saturation intensity of 0.82 MHz. Owing to their narrow linewidth, these NIR SQEs reach saturation intensities of nearly 1 MHz under non-resonant excitation, which is on par with the brightest hBN SQEs reported to date without any optical-cavity enhancement [13]. We then perform polarization-resolved PL measurements to characterize the SQE polarizability where we observe high visibilities for both the absorption and emission dipoles alongside a distinct misalignment between them (Supplementary Note 4).

The excited-state lifetime of the same SQE was extracted by performing time-resolved PL dynamics of the SQE using a pulsed laser excitation at 660 nm, resulting in an SQE radiative recombination lifetime of 1.74 ns (Supplementary Note 3). SQEs measured from different samples have similar excited-state lifetimes on the order of $\sim 1\text{--}2$ ns (Supplementary Note 3). This reaffirms that these SQEs have the potential for high brightness up to the GHz range, due to their high intrinsic recombination decay rate.

For the analysis of the ZPL distribution, we locate over 200 NIR SQEs across 5 different hBN flakes, all having undergone the same process undergoing 660 nm pump excitation (Supplementary Note 3). Here, we observe a Gaussian distribution forming with an average ZPL emission of $782 \text{ nm} \pm 36 \text{ nm}$. We note that with this fabrication process, we observe a few occurrences of SQEs in the visible spectrum across 550 nm - 700 nm, which have been associated with a boron vacancy, nitrogen vacancy, or carbon-related defect complexes [33, 34]. However, we

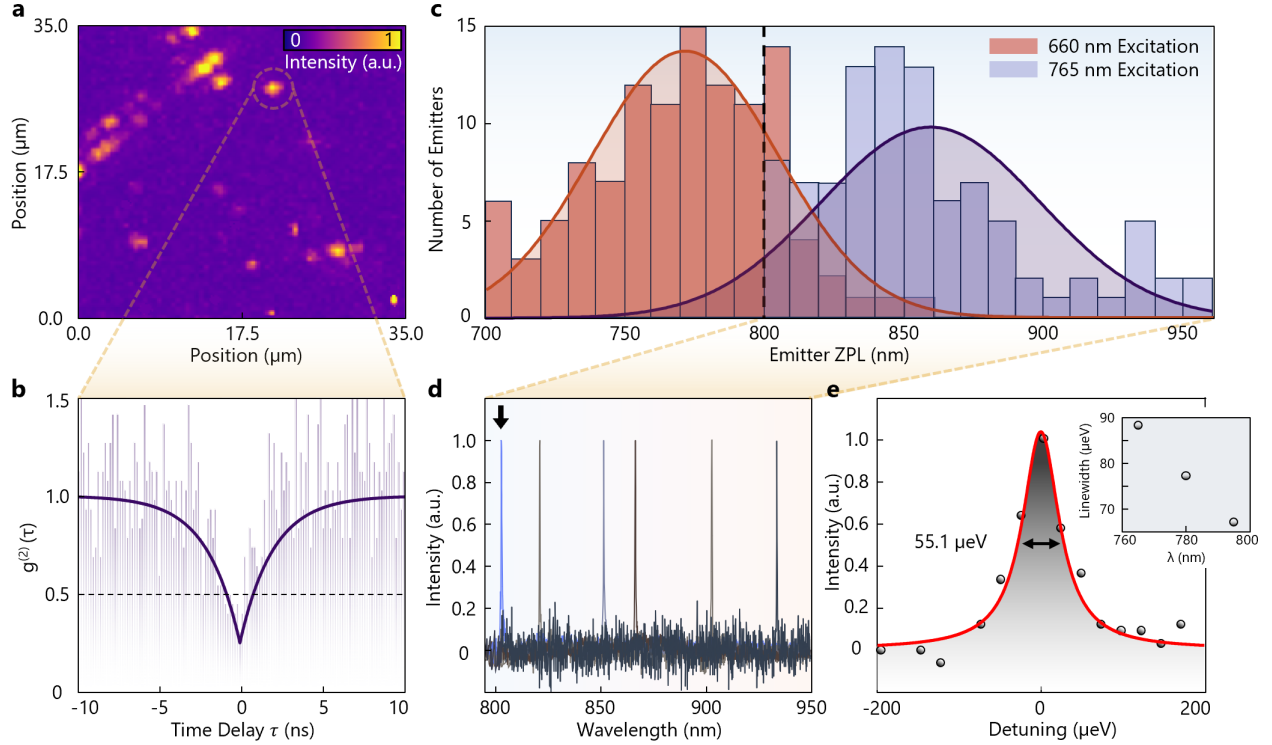


FIG. 2. Characterization of NIR SQEs. (a) A confocal hyperspectral PL map at 4 K of a processed hBN sample. Local hotspots indicate spatially isolated NIR SQEs. (b) A select SQE is highlighted and indicated by the dashed circle in panel (a). The second-order autocorrelation function of the selected NIR SQE demonstrates photon anti-bunching with a raw $g^{(2)}(0)$ value of 0.23 ± 0.09 . (c) A histogram of spatially isolated single emitters from processed hBN sample in (a) and (b) displaying the span of ZPL wavelengths observed. The orange (blue) bins indicate the span of all isolated single emitters found under 660 nm (765 nm) pump excitation. A Gaussian fit indicates a center wavelength of 770 ± 33 and 856 ± 38 nm for 660 nm and 765 nm pump excitation, respectively. The dashed line represents the spectral location of a 800 nm longpass filter to reject the 765 nm pump laser (d) Representative PL spectra of spatially isolated NIR single emitters under 765 nm pump excitation. SQEs display spectral inhomogeneity spanning over a range of wavelengths spanning from 800 nm to 960 nm. (e) Quasi-resonant excitation of an NIR SQE with a ZPL of 801 nm indicated by arrow in (d) under 795 nm pump. A spectrometer-limited FWHM of $55.1 \mu\text{eV}$ (13.3 GHz) under pump power of $148 \mu\text{W}$ is extracted. The inset displays the linewidth dependence of the SQE on laser excitation wavelength from 765 nm to 795 nm under $550 \mu\text{W}$ pump power.

observe a high density of single defect quantum emission above 800 nm, reaching ZPL wavelengths up to 960 nm, which has not been previously reported. Similar to hBN SQEs in the visible spectrum, we suspect the large spectral inhomogeneity of these NIR SQEs to arise from each single defect experiencing a variation in its local environment such as variable local deformation potentials due to the high strain coupling of atomically thin hBN flakes.

We next examined the same emitters under optical pumping at excitation wavelengths closer to the average ZPL distribution, approaching quasi-resonant excitation utilizing a wavelength tunable 780 nm laser. Performing PL confocal mappings on a singular processed hBN flake, we obtain maps under 660 and 765 nm excitation of the same raster area as displayed in Supplementary Note 5. We observe the activation of NIR SQEs under 765 nm pump excitation that had previously remained in a dark state under 660 nm pump excitation. The distribution of all single emitters detected under 660 nm excitation (orange bins) for the hBN flake is shown in

Supplementary Note 5, and an average ZPL emission of 770 ± 33 nm is extracted (see Fig. 2c). Collecting the same statistics under 765 nm excitation (blue bins), we observe an average ZPL emission of 856 ± 38 nm (see Fig. 2c). Our hypothesis, consistent with our first-principles modeling, is that the red shift in the average ZPL from 660 nm to 765 nm excitation is due to a “bright state” activation of SQEs emitting in the > 800 nm spectral band that were previously “dark” or in lower densities under 660 nm excitation, as shown in Fig. 2c. We also investigate the polarization dynamics under both pumping conditions, where we observe lower misalignment between the absorption and emission dipoles for the 765 nm excitation compared to 660 nm excitation (Supplementary Note 4). We suspect this behavior arises from two related defects, $\text{O}_\text{N}\text{V}_\text{N}$ and $\text{O}_\text{N}\text{V}_\text{N}\text{H}$, supported by our modeling described in the following sections.

Next, we perform studies on the linewidth dependence on the excitation wavelength utilizing the same tunable 780 nm laser. Figure 2d highlights the representative

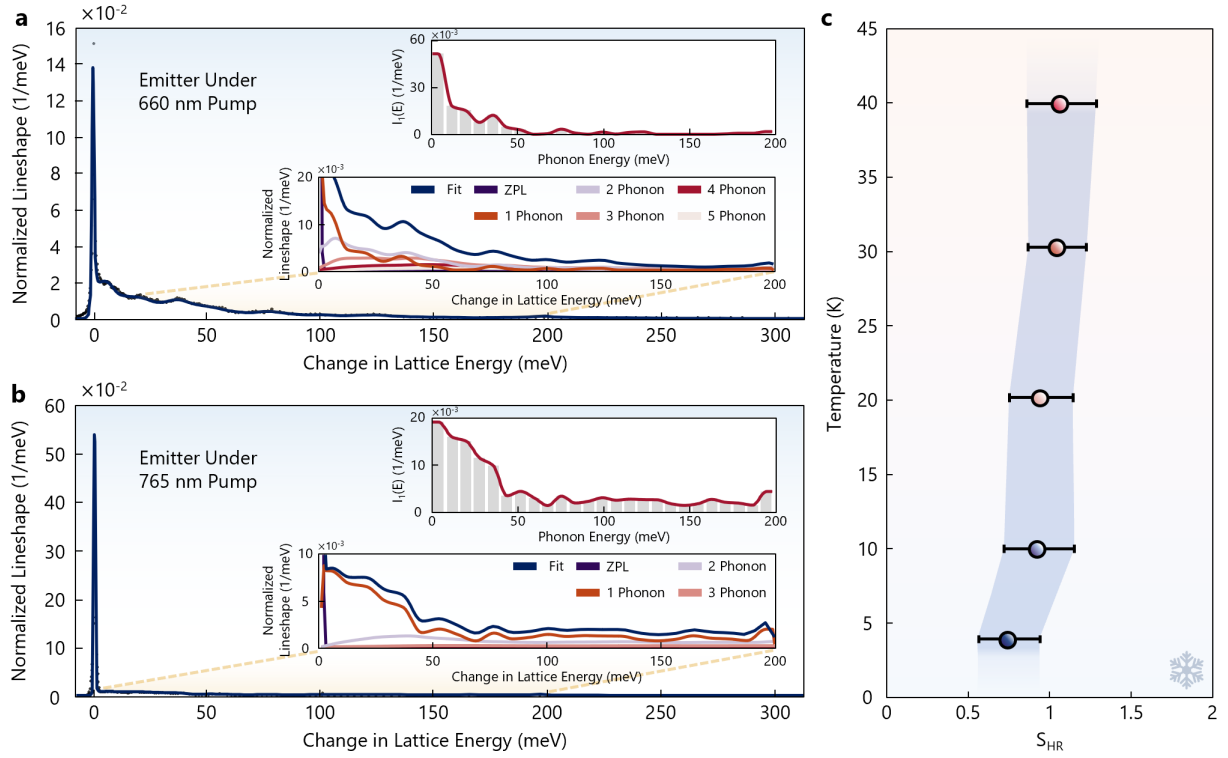


FIG. 3. **Electron-Phonon Coupling** (a) Normalized lineshape $L(\Delta E)$ of a SQE excited under 660 nm pump with a fitted ZPL at 791.3 nm (1.567 eV). Bottom inset shows the zoom-in of the PSB with the n -phonon spectral distribution decomposition with an extracted S_{HR} of 2.14 ± 0.40 . Top inset shows the 1-phonon vibronic coupling probability distribution function. (b) Normalized lineshape $L(\Delta E)$ of a SQE excited under 765 nm pump with a fitted ZPL at 859.9 nm (1.442 eV). Bottom inset shows the zoom-in of the PSB with the n -phonon spectral distribution decomposition with an extracted S_{HR} of 0.72 ± 0.12 . Top inset shows the 1-phonon vibronic coupling probability distribution function. (c) Temperature dependent Huang-Rhys analysis of the SQE under 765 nm pump in (b). Extracted S_{HR} at each temperature fall within one confidence interval of each other indicating temperature independent electron-phonon coupling strength over 4-40 K.

spectral variety of single emitters at 4 K under 765 nm excitation collected from Fig. 2c. We observe a decrease in the linewidth of the SQEs under 765 nm excitation compared to previous SQEs displayed in Fig. 1e under 660 nm excitation. Fixing the excitation wavelength at 795 nm, we conduct a quasi-resonant excitation of a representative single emitter with ZPL at 801 nm indicated by the arrow in Fig. 2d. We extract a spectrometer-limited linewidth of $55.1 \mu\text{eV}$ under a pump power of $150 \mu\text{W}$, where correcting for the IRF yields an ultrasharp linewidth of $11.1 \mu\text{eV}$ (2.7 GHz). The inset displays a linewidth dependence of the same SQE on the excitation laser as it is tuned from 765 nm to 795 nm at a constant pump power of $400 \mu\text{W}$. Here, we observe a decrease of the FWHM as the excitation wavelength approaches near resonance of the ZPL, which we attribute to a continuous suppression of spectral diffusion on fast time scales that arise from the sensitivity of the SQE to local charge fluctuations due to the DC-Stark effect. The fitted lineshape dependence on excitation wavelength from this SQE is shown in Supplementary Note 5. Earlier studies have already verified that spectral-diffusion can be strongly suppressed when hBN SQEs are driven either strictly at resonance [35, 36] or through anti-Stokes schemes [37];

here we show that for these SQEs, linewidth reduction also occurs in the quasi-resonant (< 40 meV detuning) range.

Electron-Phonon Coupling The electron-phonon coupling of individual NIR SQEs is analyzed using a finite-temperature Huang-Rhys vibronic model previously developed for hBN defects [38, 39]. In this framework, the PL spectrum of a defect is determined by the coupling between the electronic transition and lattice vibrations of the host crystal resulting in a sharp ZPL with PSBs on the low-energy side arising from multi-phonon emission processes. In the normalized PL lineshape fits, we extract the Huang-Rhys factor, S_{HR} , which represents the average number of phonons involved in the emission event using the free parameters of ZPL energy and width, and the discretized one-phonon coupling spectrum from which the full set of I_n is constructed. A complete description of the spectral transformations, finite-temperature corrections, and fitting procedure is provided in the Methods section.

Figure 3a shows the resulting fit for a SQE excited with 660 nm pump with a fitted ZPL of 791.3 nm (1.567 eV). The main panel displays the normalized lineshape

$L(\Delta E)$ together with the best-fit decomposed into ZPL and multi-phonon contributions. The lower inset highlights the individual n -phonon components, while the upper inset shows the extracted one-phonon probability distribution $I_1(\Delta E)$. For this SQE, we obtain a Huang–Rhys factor $S_{\text{HR}} = 2.14 \pm 0.4$ indicating that, on average, just over two phonons are involved in each emission event, which is consistent with relatively strong coupling to lattice vibrations. We then perform the same analysis on two additional SQEs excited at 660 nm to obtain an average Huang–Rhys factor $S_{\text{HR}} = 1.70 \pm 0.16$. The corresponding fits are provided in Supplementary Note 6. Fig. 3b presents the same analysis for a second SQE excited with 765 nm pump with a fitted ZPL of 859.9 nm (1.442 eV). The overall lineshape and its phonon-resolved decomposition are again well described by the model, but the extracted Huang–Rhys factor is significantly smaller, $S_{\text{HR}} = 0.72 \pm 0.12$. In the corresponding $I_1(\Delta E)$ panel, the features have lower probability densities and a modified spectral structure, consistent with a reduced overall strength of the one-phonon coupling and hence noticeably weaker vibronic coupling compared to the 660 nm pumped SQEs. Applying this procedure to two further SQEs excited at 765 nm yields an average Huang–Rhys factor $S_{\text{HR}} = 1.04 \pm 0.10$, with full fits shown in Supplementary Note 6. Taken together, these measurements show that SQEs addressed at 765 nm on average exhibit weaker vibronic coupling than those addressed at 660 nm.

In Fig. 3c, we apply the same fitting procedure to temperature-dependent spectra of the 765 nm emitter from Fig. 3b over the range 4–40 K. For each temperature we independently fit the full lineshape to extract $S_{\text{HR}}(T)$. The resulting values cluster within a 3σ confidence interval, showing no systematic trend with temperature. This behavior has several important implications. First, it confirms that the electron–phonon coupling is temperature independent in this range where the S_{HR} encodes the structural displacement between the ground- and excited-state lattice configurations, and the absence of any change in S_{HR} indicates that the defect does not undergo structural rearrangements, phase transitions, or “softening” as the sample is warmed from 4 to 40 K. Second, any observed evolution of the spectrum with temperature must therefore arise from changes in phonon occupation and from additional homogeneous broadening or dephasing, all of which are explicitly included in our model via the Bose–Einstein factors and the temperature-dependent ZPL width, further discussed in the next section. Third, the lack of a temperature dependence in S_{HR} over a range where $k_{\text{B}}T$ is much smaller than typical optical-phonon energies is consistent with a picture in which the dominant vibronic coupling involves higher-energy phonon modes rather than very low-energy acoustic modes. Finally, the invariability of S_{HR} demonstrates that the intrinsic defect–phonon coupling strength is robust against modest temperature drifts, underscoring the stability of this emitter for cryogenic-temperature

quantum optics applications.

Power and Temperature Broadening Dynamics. With the sharp linewidths of our NIR SQEs, we next perform an extensive linewidth characterization at cryogenic temperatures. To extract the linewidth, we fit the experimental data with a Lorentzian function. In Fig. 4a, we show a representative NIR SQE at 4 K with a linewidth of 148 μeV (104 μeV under IRF correction) under low optical excitation power of 40 μW compared to power-broadend linewidth of 279 μeV (235 μeV under IRF correction) under high optical excitation power of 3.4 mW.

We also examined pump power broadening of four NIR SQEs, shown in Fig. 4b. We fit the experimental data to a two-level pump power broadening system and extract the dephasing-limited zero-pump power linewidth, Γ_0 , and the saturation pump power, P_0 :

$$\Gamma = \Gamma_0(1 + P/P_0)^{1/2} \quad (1)$$

From our fits, we obtain raw Γ_0 of 103.8, 122.6, 124.5, and 244.8 μeV from bottom to top respectively in Fig. 4c, corresponding to IRF corrected values of 59.8, 78.6, 80.5, and 200.8 μeV . The fitted lineshapes from these select SQEs are shown in Supplementary Note 5. These values are significantly lower than reported linewidth values for non-resonant excitation of typically several meV for SQEs that emit in the visible spectrum, and once again, a distinct feature of these oxygen-related NIR SQEs.

Figure 4c first shows the temperature dependent spectra at room temperature (300 K) and cryogenic temperature (4 K) of a representative NIR SQE with a ZPL at 775 nm which verifies the room-temperature operation under ambient conditions (Supplementary Note 2).

The temperature dependent linewidth of a representative NIR SQE is shown in Fig. 4d using an optical pump power of 500 μW . At the power indicated by the arrow in Fig. 4b, we measure the temperature dependence, shown in Fig. 4d), and fit the data to a least squares residual that follows the form:

$$\Gamma(T) = \Gamma_0 + aT + bT^5 \quad (2)$$

where we only consider phonon processes involving the linear and quadratic electron-phonon coupling terms which is valid for hBN due to its weak interactions with acoustic phonon processes [40] as evidenced in the analysis of Fig. 3. Here, the red shaded region in Fig. 4d represents the IRF. The blue shaded region represents the homogeneous broadening that sets the natural linewidth alongside the inclusion of inhomogeneous broadening mechanisms due to spectral diffusion on a fast time scale. These two regions contribute to the extracted zero-temperature linewidth Γ_0 . As temperature initially increases, we observe the prominence of acoustic phonon processes from the piezoelectric coupling of hBN

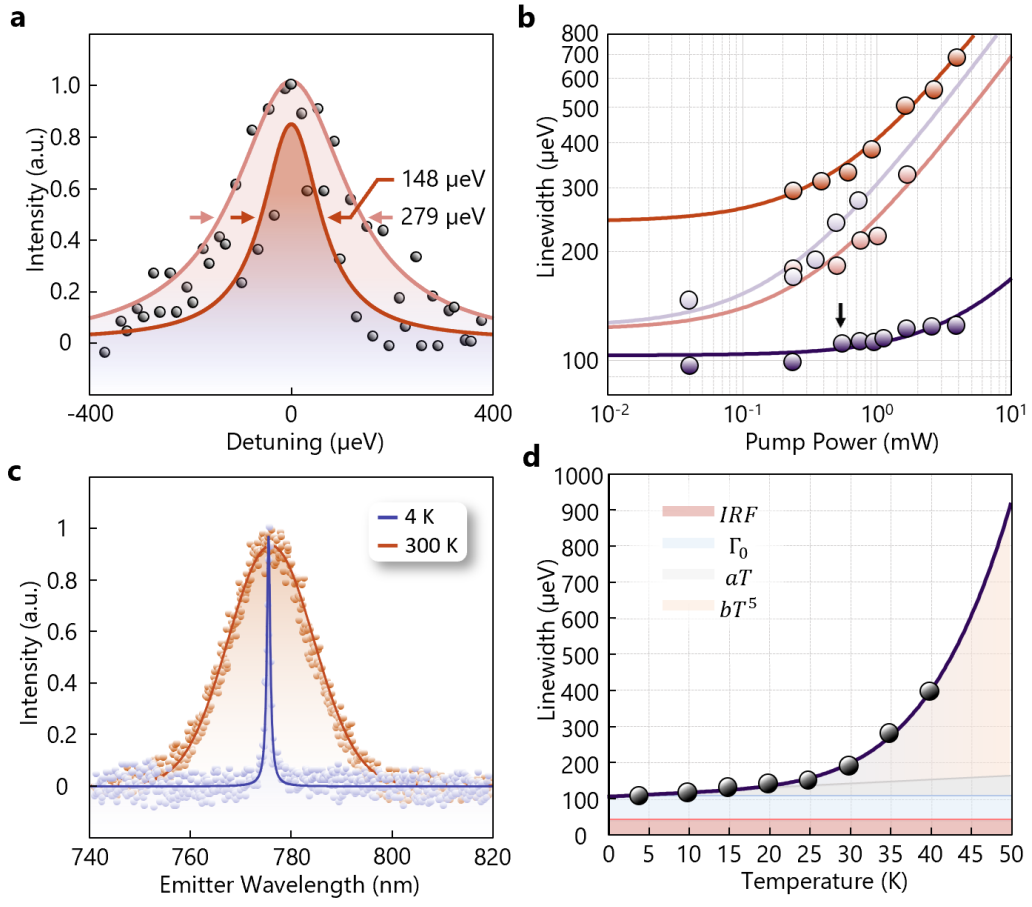


FIG. 4. Non-resonant excitation linewidth characterization. (a) A representative linewidth of an NIR SQE at 4 K under 40 μW of pump power with a spectrometer-limited FWHM of 148 μeV compared to the same SQE under 3.4 mW of pump power with a spectrometer-limited FWHM of 279 μeV both under non-resonant pump excitation at 660 nm. (b) Linewidth power-broadening dependence of multiple NIR SQEs at 4 K. A two-level system power broadening model is fit to the experimental data points. (c) PL spectra of the representative SQE shown at both 4 K and 300 K. (d) Temperature-dependence of linewidth of a specific SQE taken under 500 μW excitation power (indicated by arrow in panel (b)). The experimental data is fit to a model based on phonon-assisted broadening mechanisms coupled to deep and isolated electronic states of the defect. Shaded regions indicate contributions from different phonon-broadening mechanisms, instrument response, and homogeneous broadening.

resulting in the linear dependence to T . Finally, as temperature continues to increase we observe deformation potential coupling which scales as T^5 . This temperature dependence of the linewidth has been reported in other visible SQEs in hBN [40] and other solid-state SQEs such as semiconductor quantum dots [41] and defects in diamond [42]. For the SQE studied in Fig. 4d, we observe a narrow linewidth of 53.3 μeV correcting for the IRF at low pump power.

First-Principles Calculations. We now employ first-principles calculations to help identify the structural and optical origins of the SQEs. We screen oxygen-related defects and complexes for ZPL energies and vibronic coupling. Select configurations were already studied in [43, 44]. The simplest candidate is substitutional oxygen on the nitrogen site (O_N). We can exclude oxygen on the boron site (O_B) because its formation energy is extremely large [43], and therefore unlikely to exist as isolated de-

fects. O_N can form complexes with an oxygen interstitial ($\text{O}_\text{N}\text{O}_i$, split interstitial), with a vacancy ($\text{O}_\text{N}\text{V}_\text{N}$, $\text{O}_\text{N}\text{V}_\text{B}$), or with carbon ($\text{O}_\text{N}\text{C}_\text{N}$ and $\text{O}_\text{N}\text{C}_\text{B}$), which commonly occurs as an unintentional impurity and has been linked to luminescence in hBN [45]. Since the sample consists of flakes that have edges or corners, we also investigate O_N in the vicinity of dangling bonds [46], either in the same plane or in a neighboring plane. In addition, hydrogen is also a ubiquitous impurity in hBN [43] and can adsorb at structural imperfections such as cracks, terraces, and folds induced by mechanical exfoliation [46] or during the RTA process. Therefore, we also consider oxygen–hydrogen complexes, including $\text{O}_\text{N}\text{H}$ and $\text{O}_\text{N}\text{V}_\text{N}\text{H}$. In total, we investigated ten defect configurations, each in all possible charge states. Results are presented in Supplementary Note 7. Among them, complexes involving O_N , nitrogen vacancies, and hydrogen emerge as the most likely candidates for the observed SQEs. In fact, the two sets of measured ZPLs can be correlated with

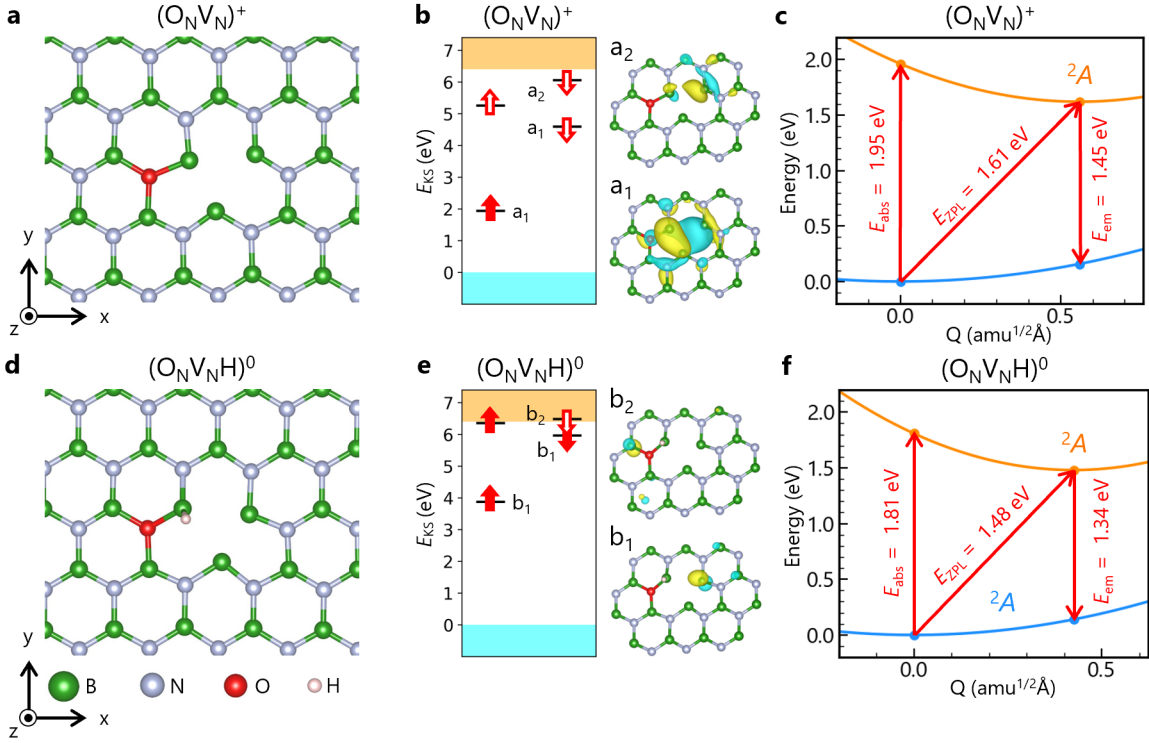


FIG. 5. Properties of the $O_N V_N$ and the $O_N V_N H$ centers. (a) Structure of $(O_N V_N)^+$. (b) Left: Kohn-Sham states for the ground state 2A of $(O_N V_N)^+$. Right: charge-density isosurfaces of the defect states of $(O_N V_N)^+$. (c) Calculated CCD for the $^2A \leftrightarrow ^2A$ transition. (d) Structure of $(O_N V_N H)^0$. (e) Left: Kohn-Sham states for the ground state 2A of $(O_N V_N H)^0$. Right: charge-density isosurfaces of the defect states of $(O_N V_N H)^0$. (f) Calculated CCD for the $^2A \leftrightarrow ^2A$ transition. The isosurface absolute value is set to $4.0 \times 10^{-8} \text{ e/a}_0^3$.

two related defects: the $O_N V_N$ and $O_N V_N H$ centers.

Our results for $O_N V_N$ are summarized in Fig. 5. The ideal, unrelaxed structure would have C_s symmetry. However, for all charge states the structures relax into lower-symmetry configurations. In the positive charge state ($(O_N V_N)^+$, Fig. 5a) the defect has C_1 symmetry and a spin-1/2 ground state denoted as the doublet 2A . The B atoms near the vacancy display a small out-of-plane distortion of about 0.3 Å. The Kohn-Sham level diagram of the 2A ground state is shown in Fig. 5b. Two states appear in the band gap. The a_1 state is a localized state formed by an antibonding combination of in-plane and out-of-plane p orbitals on the B atoms, with a small contribution from the O p orbital. The a_2 state is mainly an in-plane p orbital on one of the B atoms near the vacancy. An internal excitation (calculated with Δ SCF [47]) can promote an electron from a_1 to a_2 where the resulting configuration is also a 2A state.

The configuration coordinate diagram (CCD) of the internal transition is shown in Fig. 5c. The calculated ZPL energy of 1.62 eV (767 nm) agrees well with the SQEs observed under excitation at 660 nm (1.88 eV), which are clustered around 1.61 eV (770 nm) as shown in Fig. 2c (orange bins). Our calculated Huang-Rhys factor, $S_{HR} = 2.43$, matches well and is slightly larger than experimental values extracted in Fig. 3a, but within

computational and experimental uncertainties. A trend of computed HR factors being larger than values extracted from experiment has been observed in previous studies [48, 49]. In addition, experimental Huang-Rhys factors tend to be underestimated due to the difficulty in distinguishing between zero-phonon photons and those coupled to low-energy acoustic phonons [50], and in identifying the full extent of the coupling to higher-energy phonons.

The computed transition dipole moment for the transition is $\mu = 0.59 \text{ e\AA}$, which leads to a radiative lifetime $\tau_{\text{rad}} = 75 \text{ ns}$. This value is larger than the experimentally measured lifetime of about 2 ns for the 770 nm emitters. The discrepancy could be partly due to the presence of a nonradiative recombination channel, which would lead to an overestimate of the radiative rate extracted from experiment, and hence an underestimation of the excited-state lifetime.

The equilibrium structure of the neutral $(O_N V_N H)^0$ complex is then shown in Fig. 5(d). The defect is structurally similar to $(O_N V_N)^+$, except that it has an additional H atom bonded to a B atom between O_N and V_N, with C_1 symmetry. $(O_N V_N H)^0$ is also a spin-1/2 center, with a doublet ground state 2A . The b_1 state (Fig. 5e) is a localized B p_z state near the V_N. The higher b_2 state, being closer to the conduction band, exhibits more

delocalized character (with a lower isosurface value) and includes contributions from the B p_z orbital near O_N. In the 2A ground state, b_1 is doubly occupied and b_2 is singly occupied. When an electron is promoted from b_1 to b_2 , the excited 2A state is formed.

The CCD of this transition is shown in Fig. 5f. The calculated ZPL energy of 1.48 eV (840 nm) with a Huang-Rhys factor $S = 1.73$ is close to the dominant emission of SQEs clustered around 1.45 eV (856 nm) that are observed under excitation at 765 nm (1.62 eV) (Fig. 2c, blue bins). The calculated Huang-Rhys factor once again matches well with the experimental observation shown in Fig. 3b.

Our computed transition dipole moment for the (O_NV_NH)⁰ transition is $\mu = 0.51$ eÅ, resulting in a radiative lifetime $\tau_{\text{rad}} = 127$ ns. This longer lifetime (slower emission rate) may explain why the (O_NV_NH)⁰ emitters are not prominently observed under shorter-wavelength (660 nm) excitation. The (O_NV_NH)⁰ emitters are observed only when the excitation energy (765 nm) is low enough not to excite the (O_NV_N)⁺ emitters. However, since our hyperspectral PL maps indicate that the two classes of emitters are not spatially co-localized, it is unlikely that they directly compete for pump power via their distinct lifetimes. Therefore, a more compelling explanation could be that the (O_NV_N)⁺ emitters are excited more efficiently at 660 nm, while the (O_NV_NH)⁰ emitters are preferentially excited at 765 nm, in line with the respective overlap of their vibronic excitation bands.

Our calculations are for O_NV_N and O_NV_NH centers in ideal hBN crystals. The flakes in actual hBN samples lead to strains and distortions that can modify the properties of the SQEs. A study on similar defects in [51] has showed that realistic distortions can shift emission energies by several 0.1 eV, explaining the spectrum of ZPL wavelengths shown in Fig. 2c. In addition, both systems are optically active and paramagnetic (spin doublets) that can be observed in ESR spectrum. These states may enable optical manipulation of the spin [52], offering the prospect of exploiting the (O_NV_N) and (O_NV_NH) centers as the first quantum defects in hBN with single-photon emission in the NIR spectrum that is naturally geared toward high transmission efficiency free-space spin-photon interfaces for quantum networking. This motivates future experimental studies to confirm the existence of ODMR in these NIR SQEs.

DISCUSSION

In summary, we have created SQEs in hBN with NIR single photon emission via a simple fabrication process utilizing an oxygen-plasma treatment. The spectra collected from > 200 individual single defect complexes from PL hyperspectral confocal mappings reveal a novel type of SQE that is characterized by emission in the 700-960

nm spectral band. Only a strong NIR emission is observed from such single defects with the inclusion of the oxygen-plasma treatment and absent in control experiments performed on reference samples. Thus, we assign such distinct NIR emission to be oxygen-related. We show that these SQEs have emission at cryogenic temperatures ranging all the way to room temperature under ambient conditions. These SQEs exhibit ultra-sharp linewidths with blinking-free emission at cryogenic temperatures approaching high brightness near ~ 1 MHz, which is comparable to the brightest hBN SQEs reported to date without optical cavity enhancement. We confirm the pronounced single-photon antibunching nature of the NIR emission with measured excited-state lifetimes on the order of $\sim 1\text{-}2$ ns. First-principles calculations support the assignment of the SQEs as O_NV_N and O_NV_NH centers as the most likely candidates. The energy level structure from our modeling indicates that both defect centers are paramagnetic with spin doublets, potentially enabling spin-optical transitions. Future experimental studies of these transitions and the spin dynamics will elucidate potential applications of spin-photon entanglement with NIR SQEs in hBN.

Towards coherent single-photon generation, we have performed an extensive linewidth characterization and observe ultrasharp emission at cryogenic temperatures with linewidths approaching ~ 11.1 μ eV (2.7 GHz) under quasi-resonant excitation, currently limited by fast-timescale spectral diffusion processes and pure dephasing. Complementary electron-phonon coupling analysis shows that SQEs addressed at 765 nm exhibit consistently lower Huang-Rhys factors than their 660 nm counterparts, indicating intrinsically weaker vibronic coupling and more ZPL-dominated emission from this subset of defects. This reduced vibronic coupling, together with the observed temperature independence of the Huang-Rhys factor from 4–40 K, points to a particularly clean and structurally robust phonon environment that is highly favorable for high-coherence single-photon generation. To further assess transform-limited linewidths, resonant excitation schemes can be employed to minimize dephasing arising from “above-band” excitation and to suppress phonon-assisted processes, as has been demonstrated for other hBN QEs [35, 53, 54]. In parallel, one can leverage the atomically thin nature of hBN to realize electrostatically gated vdW heterostructure devices in which the quantum defects are embedded for dynamic charge-state control and carrier sweep-out, as recently shown for spectrally broader visible SQEs with linewidths approaching 1 meV [55]. Our oxygen-related NIR SQEs, with their order-of-magnitude narrower linewidths, are particularly well suited to such architectures, enabling more efficient suppression of spectral diffusion at lower gate voltages and deterministic coupling to nanophotonic cavities for Purcell enhancement and order-of-magnitude reductions in T_1 , as demonstrated in our prior work [15]. Overall, the oxygen-plasma treatment combined with a standard solvent clean and thermal anneal produces a

distinct class of oxygen-related hBN QEs emitting in the 700–960 nm range, opening a practical route to engineering oxygen into hBN to reliably create these defects and positioning this vdW platform for future heterostructure and cavity-integrated devices that can deliver highly coherent, indistinguishable single photons in the NIR for free-space quantum communication and networking.

METHODS

A. Sample Preparation

A standard solvent cleaning procedure is first used to remove organic residue from the surface (Fig. 1a I). Next, an oxygen plasma treatment is performed on the hBN flakes under a low vacuum environment (300 mT) at 100 W for 1 minute to introduce oxygen impurities and vacancies at the surface and within the flakes (Fig. 1a II). Finally, a high temperature RTA is performed under a nitrogen gas (N_2) and forming gas (90% N_2 , 10% H_2) environment at 1000 °C for 20 minutes to allow the thermal relaxation of strain in the hBN flakes from the mechanical exfoliation process while also promoting the diffusion of oxygen and other impurities into the hBN to generate thermodynamically stable oxygen-related defect complexes that feature NIR emission (Fig. 1a III).

B. Optical Characterization

A 660 nm continuous-wave PicoQuant laser diode and 780 tunable Toptica laser are used for steady-state PL measurements. A dichroic mirror at 680 nm cut-on and 70:30 beamsplitter is used to separate the optical excitation and collection paths for the 660 nm and 780 nm tunable laser, respectively. An additional 700 nm and 800 nm cut-on long-pass optical filter is used in the collection path to further extinguish the 660 nm and 780 nm tunable excitation laser, respectively, in the collection path. An infinity-corrected 0.42 NA NIR objective with 17 mm working distance is used for spectroscopy measurements. Our hBN samples are cooled to 4 K inside a Montana Instruments S200 cryostation and optical spectra are acquired using a Princeton Instruments HRS-500 spectrophotometer with 300/1200/1800 groove/mm gratings and a thermoelectrically-cooled Pixis Silicon CCD.

Second-order autocorrelation measurements with continuous-wave optical excitation are performed by utilizing the spectrophotometer as a monochromator to filter the emission from individual SQEs. The optical signal is then collected into a multimode fiber and HBT interferometry is performed using a broadband fiber-based beam splitter and two Excelitas SCPM-AQRH-13-FC single-photon avalanche detectors. Swabian Instruments time tagging electronics are used for photon counting and correlation. Furthermore, time-resolved PL measurements are performed using pulsed operation mode of the 660 nm laser diode with a

80 MHz repetition rate.

Polarization-resolved PL is conducted by modifying the steady-state PL setup with polarization optics. To measure the defect's absorption dipole, a linear polarizer and half-wave plate are placed in the excitation path. The polarizer is set to maximize the optical power of the excitation laser, and the half-wave plate then rotates the input excitation beam. To measure the defect's emission dipole, a linear polarizer is placed in the collection path and aligned to maximize the efficiency of our spectrophotometer. A half-wave plate is then placed prior to the polarizer and allows us to sweep through the defect's emission spectrum.

C. Finite-Temperature Phonon Sideband Analysis

We analyze the phonon sidebands using a finite-temperature Huang–Rhys model adapted from [38, 39]. Measured PL spectra $I(\lambda)$ is collected (wavelength-dependent detection efficiency calibrated with broadband light source) and then re-binned to give a spectral distribution $S(\lambda)$. We convert to photon energy $E = hc/\lambda$ and define $S(E)$ such that $S(E) dE = S(\lambda) d\lambda$, which introduces the usual Jacobian factor. To remove the E^3 dependence of the radiative density of states, we work with the normalized lineshape

$$L(E) = \frac{S(E)}{E^3}, \quad (3)$$

which isolates the intrinsic defect–phonon lineshape. In converting between these representations we propagate uncertainties from photon shot noise, detector background, and slow spectral drifts, and we adjust the energy binning to maintain approximately uniform error bars across the fitted range.

Following the Maradudin–Davies treatment of vibronic transitions in solids [56, 57], we model $L(E)$ in terms of a ZPL and a PSB. The total spectrum as a function of lattice energy change $\Delta E = E_{\text{ZPL}} - E$ is written as

$$L(\Delta E) = e^{-S_{\text{HR}}} I_0(\Delta E) + (I_0 \otimes I_{\text{PSB}})(\Delta E), \quad (4)$$

where S_{HR} is the Huang–Rhys factor, $I_0(\Delta E)$ is the normalized ZPL lineshape, and I_{PSB} is the PSB in the limit of a delta-function ZPL where \otimes denotes convolution. The PSB is expanded into contributions from processes involving n phonons,

$$I_{\text{PSB}}(\Delta E) = \sum_n e^{-S_{\text{HR}}} \frac{S_{\text{HR}}^n}{n!} I_n(\Delta E), \quad (5)$$

where the I_n are normalized n -phonon probability distributions constructed recursively as $I_n = I_1 \otimes I_{n-1}$ for $n > 1$. Finite temperature enters through the one-phonon distribution I_1 , which we express in terms of an

underlying phonon spectral function $S(E)$ and the Bose-Einstein occupation $n(E, T) = 1/(\exp(E/k_B T) - 1)$ as

$$I_1(E) = \begin{cases} A[n(E, T) + 1]S(E), & E > 0, \\ A n(|E|, T) S(|E|), & E < 0, \end{cases} \quad (6)$$

with A chosen so that $\int I_1(E) dE = 1$. Here $E > 0$ corresponds to phonon emission and $E < 0$ to phonon absorption, i.e., energy transferred from or to the lattice, respectively.

In practice, the phonon spectral function $S(E)$ is treated as an unknown function on the interval $0 \leq E \leq E_{\max}$, where E_{\max} is taken to be the maximum relevant phonon energy in hBN (~ 200 meV). We parameterize $S(E)$ by its values on a discrete energy grid $E_i = (i + \frac{1}{2})\delta E$ with step δE , and linearly interpolate between grid points. The free parameters in each fit are then the ZPL energy E_{ZPL} , the ZPL width Γ_{ZPL} , the Huang-Rhys factor S_{HR} , and the set of discrete values $\{S(E_i)\}$. We perform weighted least-squares fits of the model $L(\Delta E)$ to the experimental lineshape, using the propagated uncertainties as weights. The resulting best-fit S_{HR} and the derived one- and multi-phonon contributions $I_n(\Delta E)$ are reported in the main text and Supplementary Information.

D. First-Principles Calculations

The calculations are based on hybrid density functional theory with projector augmented wave (PAW) potentials [58], as implemented in VASP [59]. The plane-wave cutoff is set to 520 eV. We use the hybrid functional of Heyd, Scuseria, and Ernzerhof (HSE) [60, 61], combined with the Grimme-D3 correction for van der Waals interactions [62]. The fraction of nonlocal Hartree-Fock exchange is set to $\alpha = 0.40$. With this value, the calculated band gap is 6.40 eV, in agreement with the experimental gap [4] when zero-point renormalization from electron-phonon interactions [63] is included. The optimized lattice parameters are $a = 2.48$ Å and $c = 6.58$ Å, in good agreement with experiment ($a = 2.50$ Å and $c = 6.65$ Å [64]). This approach has been extensively tested, both in this work and in previous studies of h-BN [43, 46]. Defects are modeled in a 240-atom conventional supercell with AA' stacking. The supercell is built from an orthorhombic cell ($a \times a\sqrt{3} \times c$) containing two primitive cells, scaled by $5 \times 3 \times 2$. Then the lattice vectors are fixed, while atomic positions around defects are relaxed until forces are below 0.01 eV/Å. Brillouin-zone sampling is performed using a single special k-point $(\frac{1}{4}, \frac{1}{4}, \frac{1}{4})$. Spin polarization is included in all calculations.

To study internal transitions we employ the Δ SCF methodology [47]. In this approach, excitation energies are obtained as total energy differences between two calculations with constrained occupations, each including full atomic relaxation. We use configuration coordi-

nate diagrams (CCDs) to examine the coupling of these electronic transitions to lattice vibrations [65] and to compute Huang-Rhys (HR) factors S within the one-dimensional approximation [66]. The electron-phonon matrix elements are obtained from wavefunction overlaps and from linear-response theory, as implemented in the NONRAD code [67].

We also study the radiative transition rate Γ_{rad} , or equivalently the radiative lifetime τ_{rad} [68, 69]:

$$\Gamma_{\text{rad}} = \frac{1}{\tau_{\text{rad}}} = \frac{n_D E_{\text{ZPL}}^3 |\mu|^2}{3\pi\epsilon_0\hbar^4 c^3}, \quad (7)$$

where ϵ_0 is the vacuum permittivity and n_D is the refractive index of h-BN. We use the experimental value $n_D = 2.4$ [70]. E_{ZPL} and μ are evaluated explicitly from first principles.

DATA AVAILABILITY STATEMENT

The data that support the findings in this study are available from the corresponding author upon reasonable request.

SUPPORTING INFORMATION AVAILABLE

- (1) Reference samples
- (2) Room-temperature and cryogenic PL confocal maps
- (3) Room-temperature emission of NIR SQEs
- (4) Photophysics
- (5) Power-dependent spectral diffusion
- (6) ZPL distribution
- (7) Polarization analysis of the absorption and emission dipoles
- (8) Polarization dynamics of additional SQEs
- (9) Quasi-resonant vs. non-resonant excitation
- (10) Non-resonant linewidth dependence
- (11) Quasi-resonant linewidth dependence
- (12) Additional electron-phonon coupling analysis (660 nm excitation)
- (13) Additional electron-phonon coupling analysis (765 nm excitation)
- (14) Formation energies of oxygen-related defect in h-BN as a function of Fermi level in N-rich and N-poor conditions
- (15) Charge-state transition levels for oxygen-related defect in hBN (Table S1)
- Calculated optical properties of oxygen-related defects in hBN

ACKNOWLEDGMENTS

S.D., S.D.P., and G.M. thank Quantum Foundry, UCSB Nanofab, NRT at UCSB for valuable input and discussions. We gratefully acknowledge support from NSF Award No. ECCS-2032272 and the NSF Quantum Foundry through Q-AMASE-i program Award No. DMR-1906325. Y.C. and C.VdW. were supported by the U.S. Department of Energy, Office of Science, National Quantum Information Science Research Centers, Co-design Center for Quantum Advantage (C2QA) under contract number DE-SC0012704. M.E.T. was supported

by the Office of Naval Research through the Naval Research Laboratory's Basic Research Program. J.A.G. and L.C.B. acknowledge support from the NSF Science and Technology Center for the Integration of Modern Optoelectronic Materials on Demand (award DMR-2019444). The research used resources of the National Energy Research Scientific Computing Center, a DOE Office of Science User Facility supported by the Office of Science of the U.S. Department of Energy under Contract No. DE-AC02-05CH11231 using NERSC award BES-ERCAP0021021.

AUTHOR CONTRIBUTIONS

S.D., and S.D.P. contributed equally to this work. G.M. conceived the experiments and supervised the project.

S.D. prepared the samples and performed the oxygen-plasma treatment, and thermal anneal. L.V. and L.J. assisted in the sample preparation. S.D. and S.D.P. performed steady-state PL spectroscopy, time-resolved PL spectroscopy, second-order auto-correlation, polarization-resolved spectroscopy, data processing, and formal analysis. Y.C., M.T., and C.VdW performed all first-principles calculations. L.C.B and J.A.G. performed the electron-phonon coupling data processing and analysis.

COMPETING INTERESTS

The authors declare no conflicts of interest.

[1] M. Turunen, M. Brotons-Gisbert, Y. Dai, Y. Wang, E. Scerri, C. Bonato, K. D. Jöns, Z. Sun, and B. D. Gerardot, Quantum photonics with layered 2d materials, *Nature Reviews Physics* **4**, 219 (2022).

[2] S. I. Azzam, K. Parto, and G. Moody, Prospects and challenges of quantum emitters in 2d materials, *Applied Physics Letters* **118** (2021).

[3] Q. Cai, D. Scullion, W. Gan, A. Falin, S. Zhang, K. Watanabe, T. Taniguchi, Y. Chen, E. J. Santos, and L. H. Li, High thermal conductivity of high-quality monolayer boron nitride and its thermal expansion, *Science advances* **5**, eaav0129 (2019).

[4] G. Cassabois, P. Valvin, and B. Gil, Hexagonal boron nitride is an indirect bandgap semiconductor, *Nature photonics* **10**, 262 (2016).

[5] C. Fournier, A. Plaud, S. Roux, A. Pierret, M. Rosticher, K. Watanabe, T. Taniguchi, S. Buil, X. Quélin, J. Barjon, *et al.*, Position-controlled quantum emitters with reproducible emission wavelength in hexagonal boron nitride, *Nature communications* **12**, 3779 (2021).

[6] A. Gottscholl, M. Kianinia, V. Soltamov, S. Orlinskii, G. Mamin, C. Bradac, C. Kasper, K. Krambrock, A. Sperlich, M. Toth, *et al.*, Initialization and read-out of intrinsic spin defects in a van der waals crystal at room temperature, *Nature materials* **19**, 540 (2020).

[7] Y. Luo, G. D. Shepard, J. V. Ardelean, D. A. Rhodes, B. Kim, K. Barmak, J. C. Hone, and S. Strauf, Deterministic coupling of site-controlled quantum emitters in monolayer wse2 to plasmonic nanocavities, *Nature nanotechnology* **13**, 1137 (2018).

[8] G. Gross, H. Moon, B. Lienhard, S. Ali, D. K. Efetov, M. M. Furchi, P. Jarillo-Herrero, M. J. Ford, I. Aharonovich, and D. Englund, Tunable and high-purity room temperature single-photon emission from atomic defects in hexagonal boron nitride, *Nature communications* **8**, 1 (2017).

[9] H. Zhao, M. T. Pettes, Y. Zheng, and H. Htoon, Site-controlled telecom-wavelength single-photon emitters in atomically-thin mote2, *Nature communications* **12**, 6753 (2021).

[10] T. T. Tran, K. Bray, M. J. Ford, M. Toth, and I. Aharonovich, Quantum emission from hexagonal boron nitride monolayers, *Nature nanotechnology* **11**, 37 (2016).

[11] T. T. Tran, C. Elbadawi, D. Totonjian, C. J. Lobo, G. Gross, H. Moon, D. R. Englund, M. J. Ford, I. Aharonovich, and M. Toth, Robust multicolor single photon emission from point defects in hexagonal boron nitride, *ACS nano* **10**, 7331 (2016).

[12] L. Gan, D. Zhang, R. Zhang, Q. Zhang, H. Sun, Y. Li, and C.-Z. Ning, Large-scale, high-yield laser fabrication of bright and pure single-photon emitters at room temperature in hexagonal boron nitride, *ACS nano* **16**, 14254 (2022).

[13] X. Xu, Z. O. Martin, D. Sychev, A. S. Lagutchev, Y. P. Chen, T. Taniguchi, K. Watanabe, V. M. Shalaev, and A. Boltasseva, Creating quantum emitters in hexagonal boron nitride deterministically on chip-compatible substrates, *Nano letters* **21**, 8182 (2021).

[14] C. Li, J. E. Froch, M. Nonahal, T. N. Tran, M. Toth, S. Kim, and I. Aharonovich, Integration of hbn quantum emitters in monolithically fabricated waveguides, *ACS photonics* **8**, 2966 (2021).

[15] K. Parto, S. I. Azzam, N. Lewis, S. D. Patel, S. Umezawa, K. Watanabe, T. Taniguchi, and G. Moody, Cavity-enhanced 2d material quantum emitters deterministically integrated with silicon nitride microresonators, *Nano Letters* **22**, 9748 (2022).

[16] D. Yamashita, M. Yumoto, A. Narazaki, and M. Okano, Deterministic integration of hbn single-photon emitters on sin waveguides via femtosecond laser processing, *arXiv preprint arXiv:2504.19477* (2025).

[17] S. D. Patel, K. Parto, M. Choquer, N. Lewis, S. Umezawa, L. Hellman, D. Polishchuk, and G. Moody, Surface acoustic wave cavity optomechanics with atomically thin h-bn and wse 2 single-photon emitters, *PRX Quantum* **5**, 010330 (2024).

[18] H. L. Stern, Q. Gu, J. Jarman, S. Eizagirre Barker, N. Mendelson, D. Chugh, S. Schott, H. H. Tan, H. Sirringhaus, I. Aharonovich, *et al.*, Room-temperature op-

tically detected magnetic resonance of single defects in hexagonal boron nitride, *Nature communications* **13**, 618 (2022).

[19] R. N. Patel, R. E. Fishman, T.-Y. Huang, J. A. Gusdorff, D. A. Fehr, D. A. Hopper, S. A. Breitweiser, B. Porat, M. E. Flatté, and L. C. Bassett, Room temperature dynamics of an optically addressable single spin in hexagonal boron nitride, *Nano letters* **24**, 7623 (2024).

[20] N. Chejanovsky, A. Mukherjee, J. Geng, Y.-C. Chen, Y. Kim, A. Denisenko, A. Finkler, T. Taniguchi, K. Watanabe, D. B. R. Dasari, *et al.*, Single-spin resonance in a van der waals embedded paramagnetic defect, *Nature materials* **20**, 1079 (2021).

[21] A. Gottscholl, M. Diez, V. Soltamov, C. Kasper, A. Sperlich, M. Kianinia, C. Bradac, I. Aharonovich, and V. Dyakonov, Room temperature coherent control of spin defects in hexagonal boron nitride, *Science Advances* **7**, eabf3630 (2021).

[22] I. O. Robertson, S. C. Scholten, P. Singh, A. J. Healey, F. Meneses, P. Reineck, H. Abe, T. Ohshima, M. Kianinia, I. Aharonovich, *et al.*, Detection of paramagnetic spins with an ultrathin van der waals quantum sensor, *ACS nano* **17**, 13408 (2023).

[23] R. Gong, G. He, X. Gao, P. Ju, Z. Liu, B. Ye, E. A. Henriksen, T. Li, and C. Zu, Coherent dynamics of strongly interacting electronic spin defects in hexagonal boron nitride, *Nature Communications* **14**, 3299 (2023).

[24] N. Mendelson, M. Doherty, M. Toth, I. Aharonovich, and T. T. Tran, Strain-induced modification of the optical characteristics of quantum emitters in hexagonal boron nitride, *Advanced Materials* **32**, 1908316 (2020).

[25] A. Branny, S. Kumar, R. Proux, and B. D. Gerardot, Deterministic strain-induced arrays of quantum emitters in a two-dimensional semiconductor, *Nature communications* **8**, 15053 (2017).

[26] K. Parto, S. I. Azzam, K. Banerjee, and G. Moody, Defect and strain engineering of monolayer wse2 enables site-controlled single-photon emission up to 150 k, *Nature communications* **12**, 3585 (2021).

[27] A. Jahid, M. H. Alsharif, and T. J. Hall, A contemporary survey on free space optical communication: Potentials, technical challenges, recent advances and research direction, *Journal of network and computer applications* **200**, 103311 (2022).

[28] B. Spokony, H. Utzat, H. Moon, G. Gross, D. Englund, and M. G. Bawendi, Effect of spectral diffusion on the coherence properties of a single quantum emitter in hexagonal boron nitride, *The journal of physical chemistry letters* **11**, 1330 (2020).

[29] S. White, C. Stewart, A. S. Solntsev, C. Li, M. Toth, M. Kianinia, and I. Aharonovich, Phonon dephasing and spectral diffusion of quantum emitters in hexagonal boron nitride, *Optica* **8**, 1153 (2021).

[30] X. Li, G. D. Shepard, A. Cupo, N. Camporeale, K. Shayan, Y. Luo, V. Meunier, and S. Strauf, Nonmagnetic quantum emitters in boron nitride with ultranarrow and sideband-free emission spectra, *ACS nano* **11**, 6652 (2017).

[31] H. Akbari, W.-H. Lin, B. Vest, P. K. Jha, and H. A. Atwater, Temperature-dependent spectral emission of hexagonal boron nitride quantum emitters on conductive and dielectric substrates, *Physical Review Applied* **15**, 014036 (2021).

[32] L. Allen and J. H. Eberly, *Optical resonance and two-level atoms* (Courier Corporation, 2012).

[33] N. Mendelson, D. Chugh, J. R. Reimers, T. S. Cheng, A. Gottscholl, H. Long, C. J. Mellor, A. Zettl, V. Dyakonov, P. H. Beton, *et al.*, Identifying carbon as the source of visible single-photon emission from hexagonal boron nitride, *Nature materials* **20**, 321 (2021).

[34] A. Sajid, J. R. Reimers, and M. J. Ford, Defect states in hexagonal boron nitride: Assignments of observed properties and prediction of properties relevant to quantum computation, *Physical Review B* **97**, 064101 (2018).

[35] T. T. Tran, M. Kianinia, M. Nguyen, S. Kim, Z.-Q. Xu, A. Kubanek, M. Toth, and I. Aharonovich, Resonant excitation of quantum emitters in hexagonal boron nitride, *Acs Photonics* **5**, 295 (2018).

[36] K. Konthasinghe, C. Chakraborty, N. Mathur, L. Qiu, A. Mukherjee, G. D. Fuchs, and A. N. Vamivakas, Rabi oscillations and resonance fluorescence from a single hexagonal boron nitride quantum emitter, *Optica* **6**, 542 (2019).

[37] T. T. Tran, C. Bradac, A. S. Solntsev, M. Toth, and I. Aharonovich, Suppression of spectral diffusion by anti-stokes excitation of quantum emitters in hexagonal boron nitride, *Applied Physics Letters* **115** (2019).

[38] A. L. Exarhos, D. A. Hopper, R. R. Grote, A. Alkauskas, and L. C. Bassett, Optical signatures of quantum emitters in suspended hexagonal boron nitride, *ACS nano* **11**, 3328 (2017).

[39] R. N. Patel, D. A. Hopper, J. A. Gusdorff, M. E. Turiansky, T.-Y. Huang, R. E. Fishman, B. Porat, C. G. Van de Walle, and L. C. Bassett, Probing the optical dynamics of quantum emitters in hexagonal boron nitride, *PRX Quantum* **3**, 030331 (2022).

[40] O. Ari, N. Polat, V. Firat, O. Cakir, and S. Ates, Temperature-dependent spectral properties of hexagonal boron nitride color centers, *ACS Photonics* **12**, 1676 (2025).

[41] L. Besombes, K. Kheng, L. Marsal, and H. Mariette, Acoustic phonon broadening mechanism in single quantum dot emission, *Physical Review B* **63**, 155307 (2001).

[42] K. D. Jahnke, A. Sipahigil, J. M. Binder, M. W. Doherty, M. Metsch, L. J. Rogers, N. B. Manson, M. D. Lukin, and F. Jelezko, Electron–phonon processes of the silicon–vacancy centre in diamond, *New Journal of Physics* **17**, 043011 (2015).

[43] L. Weston, D. Wickramaratne, M. Mackoit, A. Alkauskas, and C. Van de Walle, Native point defects and impurities in hexagonal boron nitride, *Physical Review B* **97**, 214104 (2018).

[44] S. Li and A. Gali, Identification of an oxygen defect in hexagonal boron nitride, *The Journal of Physical Chemistry Letters* **13**, 9544 (2022).

[45] M. Mackoit-Sinkevičienė, M. Maciaszek, C. G. Van de Walle, and A. Alkauskas, Carbon dimer defect as a source of the 4.1 ev luminescence in hexagonal boron nitride, *Applied Physics Letters* **115** (2019).

[46] M. E. Turiansky, A. Alkauskas, L. C. Bassett, and C. G. Van de Walle, Dangling bonds in hexagonal boron nitride as single-photon emitters, *Physical review letters* **123**, 127401 (2019).

[47] R. O. Jones and O. Gunnarsson, The density functional formalism, its applications and prospects, *Reviews of Modern Physics* **61**, 689 (1989).

[48] L. Razinkovas, M. W. Doherty, N. B. Manson, C. G. Van de Walle, and A. Alkauskas, Vibrational and vibronic structure of isolated point defects: The nitrogen-vacancy center in diamond, *Physical Review B* **104**, 045303 (2021).

[49] M. E. Turiansky and J. L. Lyons, Approximate excited-state potential energy surfaces for defects in solids, *Physical Review B* **112**, 205401 (2025).

[50] N. R. Jungwirth, B. Calderon, Y. Ji, M. G. Spencer, M. E. Flatté, and G. D. Fuchs, Temperature dependence of wavelength selectable zero-phonon emission from single defects in hexagonal boron nitride, *Nano letters* **16**, 6052 (2016).

[51] M. E. Turiansky and C. G. Van de Walle, Impact of dangling bonds on properties of h-bn, *2D Materials* **8**, 024002 (2021).

[52] K. Czelej, M. E. Turiansky, S. Mu, and C. G. Van de Walle, Scandium-based point defect in aln for quantum information processing, *Physical Review B* **110**, 125116 (2024).

[53] A. Dietrich, M. Bürk, E. S. Steiger, L. Antoniuk, T. T. Tran, M. Nguyen, I. Aharonovich, F. Jelezko, and A. Kubanek, Observation of fourier transform limited lines in hexagonal boron nitride, *Physical Review B* **98**, 081414 (2018).

[54] C. Fournier, K. Watanabe, T. Taniguchi, J. Barjon, S. Buil, J.-P. Hermier, and A. Delteil, Investigating the fast spectral diffusion of a quantum emitter in hbn using resonant excitation and photon correlations, *Physical Review B* **107**, 195304 (2023).

[55] S. J. White, T. Yang, N. Dotschuk, C. Li, Z.-Q. Xu, M. Kianinia, A. Stacey, M. Toth, and I. Aharonovich, Electrical control of quantum emitters in a van der waals heterostructure, *Light: Science & Applications* **11**, 186 (2022).

[56] A. Maradudin, Theoretical and experimental aspects of the effects of point defects and disorder on the vibrations of crystals—1, in *Solid state physics*, Vol. 18 (Elsevier, 1966) pp. 273–420.

[57] G. Davies, Vibronic spectra in diamond, *Journal of Physics C: Solid state physics* **7**, 3797 (1974).

[58] P. E. Blöchl, Projector augmented-wave method, *Physical review B* **50**, 17953 (1994).

[59] G. Kresse and J. Furthmüller, Efficient iterative schemes for ab initio total-energy calculations using a plane-wave basis set, *Physical review B* **54**, 11169 (1996).

[60] J. Heyd, G. E. Scuseria, and M. Ernzerhof, Hybrid functionals based on a screened coulomb potential, *The Journal of chemical physics* **118**, 8207 (2003).

[61] H. J. S. Ge and M. Ernzerhof, Erratum: “hybrid functionals based on a screened coulomb potential” [j. chem. phys. 118, 8207 (2003)], *J. Chem. Phys* **124**, 219906 (2006).

[62] S. Grimme, J. Antony, S. Ehrlich, and H. Krieg, A consistent and accurate ab initio parametrization of density functional dispersion correction (dft-d) for the 94 elements h-pu, *The Journal of chemical physics* **132** (2010).

[63] G. Antonius, S. Poncé, E. Lantagne-Hurtubise, G. Auclair, X. Gonze, and M. Côté, Dynamical and anharmonic effects on the electron-phonon coupling and the zero-point renormalization of the electronic structure, *Physical Review B* **92**, 085137 (2015).

[64] Y. Gu, M. Zheng, Y. Liu, and Z. Xu, Low-temperature synthesis and growth of hexagonal boron-nitride in a lithium bromide melt, *Journal of the American Ceramic Society* **90**, 1589 (2007).

[65] C. E. Dreyer, A. Alkauskas, J. L. Lyons, A. Janotti, and C. G. Van de Walle, First-principles calculations of point defects for quantum technologies, *Annual Review of Materials Research* **48**, 1 (2018).

[66] A. Alkauskas, J. L. Lyons, D. Steiauf, and C. G. Van de Walle, First-principles calculations of luminescence spectrum line shapes for defects in semiconductors: the example of gan and zno, *Physical review letters* **109**, 267401 (2012).

[67] M. E. Turiansky, A. Alkauskas, M. Engel, G. Kresse, D. Wickramaratne, J.-X. Shen, C. E. Dreyer, and C. G. Van de Walle, Nonrad: Computing nonradiative capture coefficients from first principles, *Computer Physics Communications* **267**, 108056 (2021).

[68] A. M. Stoneham, *Theory of defects in solids: electronic structure of defects in insulators and semiconductors* (Oxford University Press, 2001).

[69] C. E. Dreyer, A. Alkauskas, J. L. Lyons, and C. G. Van de Walle, Radiative capture rates at deep defects from electronic structure calculations, *Physical Review B* **102**, 085305 (2020).

[70] G. Cappellini, G. Satta, M. Palummo, and G. Onida, Optical properties of bn in cubic and layered hexagonal phases, *Physical Review B* **64**, 035104 (2001).